Coarse-grained equivalent stiffness: A structure-plasticity indicator across the order-disorder spectrum

Chen-Wei Bian,[1] Lin-Li Cao,[2] Rong-Hao Shi,[1,3,*] Daniel Şopu,[3,4,†] and Yun-Jiang Wang[2,‡]

[1]*Henan Key Laboratory of Advanced Conductor Materials, Institute of Materials, Henan Academy of Sciences, Zhengzhou 450046, China*

[2]*State Key Laboratory of Nonlinear Mechanics, Institute of Mechanics, Chinese Academy of Sciences, Beijing 100190, China*

[3]*Erich Schmid Institute of Materials Science, Austrian Academy of Sciences, Leoben 8700, Austria*

[4]*Materials Modelling, Institute of Materials Science, Technical University of Darmstadt, Darmstadt 64287, Germany*

(Received 24 December 2025; revised 29 April 2026; accepted 12 May 2026; published 1 June 2026)

Predicting plastic deformation across the spectrum of structural order, from crystalline to amorphous solids, remains a grand challenge. Coarse-grained equivalent stiffness (CGES), derived from the local dynamical matrix, is introduced as a broadly applicable parameter for mechanical stability. Its spatial variation effectively pinpoints "soft zones" susceptible to plastic rearrangements. Across six systems ranging from single crystals with dislocations to disordered polycrystals, quasicrystals, and amorphous solids, CGES spatially correlate with local plastic rearrangements, accurately capturing dislocation cores, grain boundaries, and shear transformation zones. In single crystals, CGES gradients deterministically pinpoint dislocation cores where plasticity is fully localized. For the four disordered systems, quantitative analysis shows that plastic events are statistically concentrated within CGES-identified soft zones, with occurrence probabilities 3–7 times higher than in the bulk. Moreover, local eigenvectors align with plastic rearrangements' directions, elucidating microscopic deformation pathways. Within the athermal quasistatic regime studied here, CGES offers an efficient structural descriptor for identifying plasticity-prone regions without prior loading, thereby helping to clarify the microscopic origins of localized failure in diverse solids.

DOI: 10.1103/qbmm-s8n5

I. INTRODUCTION

The mechanism of plastic deformation and failure in solids materials has long been a central topic in solid mechanics, materials science, and condensed matter physics. For crystals, plastic deformation is essentially deterministic and primarily mediated by defects such as dislocations, disclinations, and twins [1]. While traditional dislocation theory remains partially applicable within individual grains of polycrystalline materials, it fails to directly describe plastic deformation in quasicrystals and amorphous solids, which lack long-range periodic structures [2]. Their plastic behaviors often exhibit highly spatially localized characteristics [3,4].

Over the past several decades, numerous structural, thermodynamic, and mechanical indicators have been proposed to pinpoint "defect" sites or "soft zones" that presage plastic events in amorphous solids. These include free volume [5–7], local excess entropy [8–11], hexatic order [12,13], soft modes [14–16], vibrality [17], local fivefold symmetry [18,19], Voronoi anisotropy [20], flexibility volume [21,22], residual plastic strength [23–25], softness [26,27], energy landscape [28–30], local thermal energy [31,32], generalized bond direction order [33], local thermal expansion coefficient [34,35], local density [36], orientational order [37], Burgers vectors [38], atomic nonaffinity [39], density of fertile sites [40,41], vortex fields [42–44], and hedgehog topological defects [45], among others.

Despite the plethora of indicators proposed over the past several decades, most remain tailored to specific structural motifs, limiting their generality. In contrast, the Burgers vector and soft modes emerge as versatile frameworks applicable to both crystalline and amorphous solids [46]. The Burgers vector quantifies amorphous topological defects within the nonaffine displacement field, enabling direct correlation with incipient plastic events. Soft modes reveal quasilocalized low-frequency vibrational modes that are strongly coupled to dislocations and shear transformation zones (STZs) [47]. Yet both approaches carry inherent limitations. Defining the Burgers vector in amorphous systems demands complete atomic displacement data, necessitating prior loading and thus compromising predictive power, while soft modes require diagonalizing the full dynamical matrix, which is a computationally intensive task for large systems. Moreover, neither framework readily extends to complex lattices such as A15-type phases or quasicrystals. This gap underscores the pressing need of preemptive defects identification and plasticity forecasting, independent of preloading or intensive computation and robust across diverse atomic arrangements.

Building on this need, a dimensionless parameter "coarse-grained equivalent stiffness" (CGES) is introduced in this

*Contact author: smartsrh@hnas.ac.cn
†Contact author: daniel.sopu@oeaw.ac.at
‡Contact author: yjwang@imech.ac.cn

Published by the American Physical Society under the terms of the Creative Commons Attribution 4.0 International license. Further distribution of this work must maintain attribution to the author(s) and the published article's title, journal citation, and DOI.

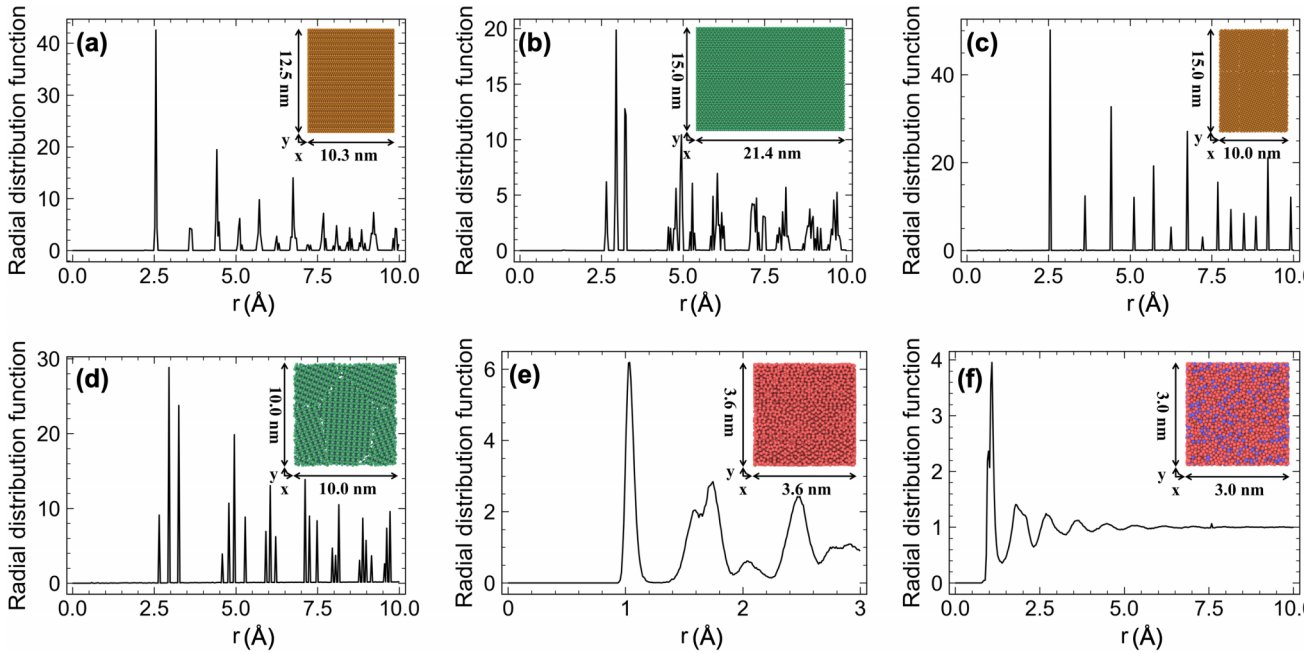


FIG. 1. RDF curves and model configurations (inset) for the (a) single-edge dislocation Cu, (b) single-edge dislocation Nb_3Sn, (c) polycrystalline Cu, (d) polycrystalline Nb_3Sn, (e) icosahedral quasicrystal, and (f) KA amorphous mixture, respectively.

work, aimed at correlating plasticity and structure across polycrystals, quasicrystals, and amorphous materials. Equivalent stiffness, derived from the local dynamical matrix, has successfully predicted the initial STZs in CuZr metallic glasses at a minimal computational cost [48,49]. Note that the computational complexity of the local dynamical matrix is $O(d^2N)$ (where d is the dimensionality and N is the number of atoms), significantly lower than the $O((dN)^2)$ required for the full dynamical matrix, highlighting the efficiency advantage of CGES over soft mode analysis.

Through systematic athermal quasistatic (AQS) shear simulations [50] and comprehensive analysis of three-dimensional (3D) models spanning single fcc and A15-type with an edge dislocation, fcc and A15-type polycrystals, quasicrystals, and amorphous materials, the ability of CGES to identify plasticity-prone regions under AQS loading is assessed across diverse atomic arrangements. Through intuitive visualizations and rigorous quantitative statistical analyses, the "soft zones," local regions exhibiting defective order and high-vibrational instability and prone to plastic rearrangement events, are precisely delineated by CGES. Furthermore, by exploring the physical significance of the local eigenvectors in soft zones, the significant directional correlation with the actual nonaffine displacement vectors is uncovered. Based on this evidence, a consistent and efficient structural tool for identifying defectlike, plasticity-prone regions under AQS loading can be formulated across diverse atomic arrangements.

II. THEORY AND SIMULATION METHODS

A. Simulation details

Single-edge dislocation and polycrystalline models of fcc Cu (lattice constant 3.615 Å) and A15-type Nb_3Sn (lattice constant 5.290 Å) were constructed using ATOMSK [51] and relaxed to minimum energy via embedded-atom method (EAM) potentials [52,53] in LAMMPS [54]. The Cu single-edge dislocation model, oriented with [110] slip, [1-11], and [1-12], contains 14 580 atoms (about $103 \times 125 \times 13$ Å^3); its A15 counterpart (oriented [100], [011], [0-11]) has 25 920 atoms (about $214 \times 149 \times 14$ Å^3). Polycrystalline Cu and A15-type Nb_3Sn contain 13 782 atoms (about $100 \times 150 \times 11$ Å^3) and 8583 atoms (about $100 \times 100 \times 16$ Å^3), respectively. Structural integrity and dislocation configurations in these systems were verified through radial distribution functions (RDFs), and atomic visualizations were performed using OVITO [55], as shown in Figs. 1(a)–1(d).

One-component 3D icosahedral quasicrystals were generated using an effective oscillating pair potential with three energy wells [56]. Systems containing 9600 atoms were equilibrated at zero pressure, a reduced density of $\rho = 0.03$, and a temperature of $T = 2.9$, for 10^4 time steps in the canonical ensemble [57] then were linearly quenched to $T = 0.18$ at a pressure of 0.1 over 6×10^7 time steps. Final inherent structures were fully relaxed by conjugate-gradient (CG) energy minimization, yielding simulation cells of approximately $36 \times 36 \times 11$ Å^3 under periodic boundary conditions. The characteristic sharp peaks and absence of translational periodicity in the RDF, together with a representative atomic configuration, are displayed in Fig. 1(e).

Amorphous solids were represented by the canonical Kob-Andersen (KA) 80:20 binary Lennard-Jones (LJ) mixture in reduced units ($\sigma_{AA} = \varepsilon_{AA} = m_A = k_B = 1$) [58]. Interaction parameters were $\sigma_{AB} = 0.8$, $\sigma_{BB} = 0.88$, $\varepsilon_{AB} = 1.5$, $\varepsilon_{BB} = 0.5$, and $m_B = 1.0$, with a cutoff of $r_c = 2.5\sigma_{ij}$. Systems of 8000 atoms were initialized with random positions, compressed, and equilibrated at high temperature ($T = 0.9 \gg$ the glass transition temperature T_g) using a soft cosine potential and then switched to the full KA potential [57]. After NPT equilibration at $T = 0.9$ and $p = 0.1$, samples were linearly

quenched to $T = 0.1$. Final structures were also fully relaxed by CG energy minimization, yielding cubic cells of about $30 \times 30 \times 8$ Å^3 (reduced density $\rho \approx 1.20$). The typical amorphous RDF profile and a snapshot of the inherent structure are presented in Fig. 1(f).

B. Coarse-grained equivalent stiffness

The local dynamical matrix was originally proposed by LeSar *et al.* [59] and subsequently applied to analyze the mechanical properties of composite materials [60]. Building on this foundation, we introduced the equivalent stiffness as a dimensionless parameter [48,49]:

$$D_i^* = \ln\left(\frac{\hbar|D_i|^{1/6}}{k_B T}\right). \tag{1}$$

Here, $\hbar$ represents the reduced Planck constant, k_B denotes the Boltzmann constant, T is the temperature, and $|D_i|$ corresponds to the local dynamical matrix determinant for atom i. The logarithm in Eq. (1) is strictly dimensionless. The local dynamical matrix for atom i is a 3×3 matrix whose elements have the dimension of (frequency)^2, i.e., (s^{-2}). Its determinant $|D_i|$ therefore carries dimensions of (frequency)^6, so that $|D_i|^{1/6}$ has the dimension of frequency (s^{-1}). Multiplying by $\hbar$ (J s) gives an energy (J), and dividing by $k_B T$ (J) yields a dimensionless ratio. Consequently, D_i^* is independent of the unit system employed. This parameter not only reflects the relative magnitude of local stiffness but also has a direct connection to the thermodynamic properties of the system.

The equivalent stiffness distribution varies with structural order. To create a continuous field for derivative analysis and average out atomic-scale fluctuations, coarse-graining is applied consistently by locally averaging over a radius of 6 Å [48]. This spatial scale is critical for capturing local correlations. Previous work on metallic glasses has demonstrated that a coarse-graining length of ∼6 Å yields the strongest correlation between vibrational anomalies and local potential energy landscape (PEL) anharmonicity, effectively bridging short- and medium-range order [61]. This radius also approximates typical interatomic potential cutoffs, capturing key local correlations without oversmoothing.

Physically, the ∼6-Å radius is supported by the spatial autocorrelation analysis of Yang *et al.* [61], who showed that the Pearson correlation coefficient between the boson peak intensity and the activation energy in the PEL is maximized at a coarse-graining length of $L \approx 5.9$ Å. At this length, the spatial autocorrelation functions of both quantities decay to $\exp(-3)$ of their reference values, representing an optimal compromise. Shorter averaging lengths lose medium-range structural correlations, whereas longer ones cause the correlation to vanish. This characteristic length encompasses both the short-range and the medium-range order of the system. For systems with significantly different lattice constants or bonding characters, we recommend performing a similar spatial autocorrelation analysis of the relevant structural property to determine the system-specific optimal coarse-graining radius, thereby facilitating the application of CGES to systems beyond those studied here while reducing possible artifacts or loss of critical local information.

In single crystals with long-range order and smooth distributions, soft zones are reliably identified by the first derivative ($\nabla \bar{D}$) of this averaged field. In contrast, for polycrystalline, quasicrystalline, and amorphous structures with inherent heterogeneity and sharper fluctuations, the divergence of the gradient is necessary to pinpoint defect-prone soft zones:

$$\nabla^2 \bar{D}^* = \bar{D}^*_{,xx} + \bar{D}^*_{,yy}. \tag{2}$$

Here, $D^*_{,xx}$ is the second derivative of CGES in the x direction, and $D^*_{,yy}$ is the second derivative of CGES in the y direction.

III. RESULTS AND DISCUSSION

A. Visual identification of soft zones

To rigorously validate the predictive capability of CGES and its divergence, single-edge dislocation models in fcc Cu and A15-type Nb_3Sn are first examined. The CGES distributions and their y-directional gradients are presented in Figs. 2(a1)–2(b2). The distinct core structures are effectively resolved by these gradient maps, capturing the dissociation into Shockley partials in Cu and the compact core in Nb_3Sn. It is revealed by comparison with the nonaffine displacement fields under 0.1% AQS shear [Figs. 2(a3) and 2(b3)] that regions of intense atomic rearrangement precisely align with the soft zones (i.e., the dislocation cores) identified by the CGES gradient. This spatial correspondence confirms that the first derivative of CGES serves as a robust predictor of dislocation-mediated plasticity in crystalline systems.

To extend this validation to increasingly disordered systems, the CGES divergence ($\nabla^2 \bar{D}^*$) is employed for polycrystalline, quasicrystalline, and amorphous models. In polycrystalline Cu and Nb_3Sn [Figs. 2(c1)–2(d3)], plastic deformation is inherently heterogeneous, concentrating near grain boundaries and triple/quadruple junctions. These topological defects are successfully captured by the CGES divergence maps [Figs. 2(c2) and 2(d2)], showing strong spatial overlap with the localized nonaffine displacement fields [Figs. 2(c3) and 2(d3)] observed under shear.

Similarly, in the icosahedral quasicrystal model [Figs. 2(e1)–2(e3)], which lacks translational periodicity, soft zones are effectively identified by the divergence. Notably, these zones correspond to vortexlike plastic rearrangements, aligning with the STZ-vortex model where STZ quadrupolar strain/stress fluctuations induce the collective vortexlike movement of atoms [43]. Finally, in the limit of maximum disorder represented by the KA amorphous system [Figs. 2(f1)–2(f3)], a distributed network of soft zones is revealed by the CGES divergence. The locations of STZs, where displacements are maximized, are roughly predicted by these zones. Collectively, it is demonstrated by these results that CGES divergence is an effective structural indicator for identifying plasticity-prone defects across a wide spectrum of structural order.

B. Quantitative determination of soft zones

The identification of soft zones relies on ranking atoms by their CGES divergence values ($\nabla^2 \bar{D}^*$). A critical parameter is the threshold divergence that delineates "soft" from "hard," which directly determines the soft zone coverage fraction,

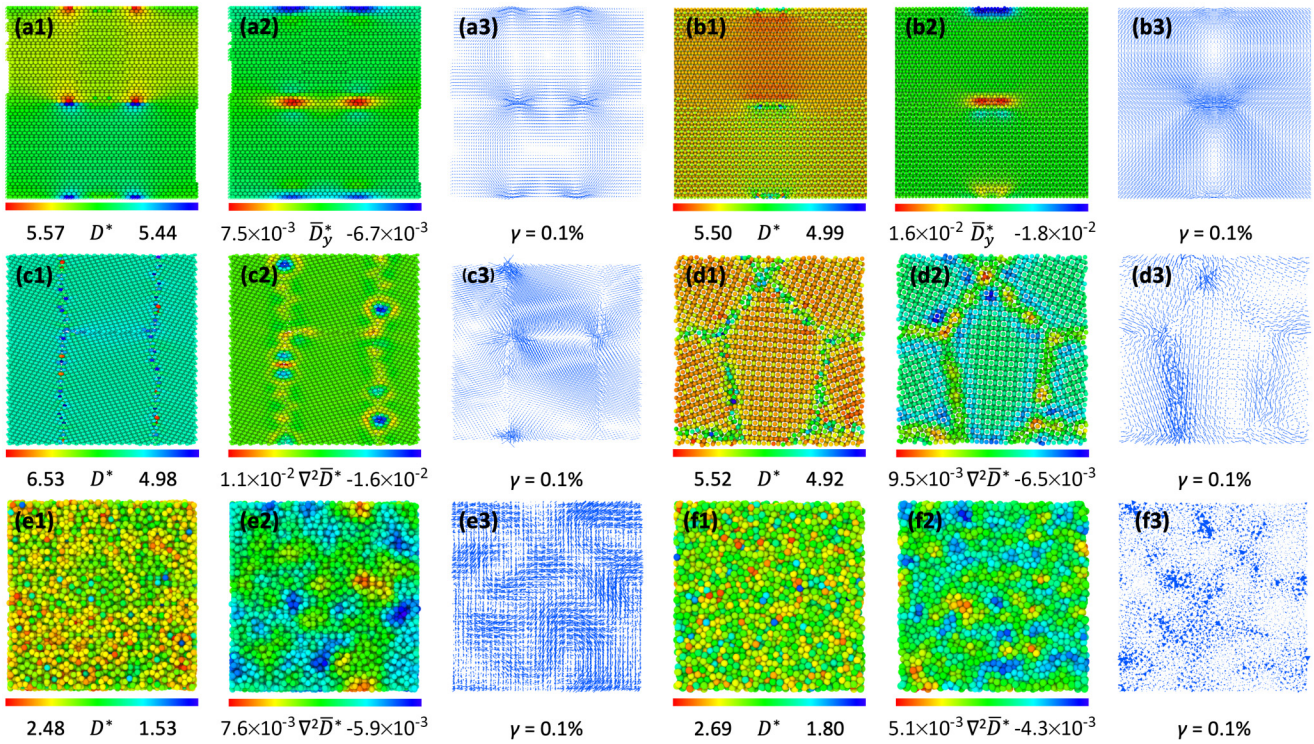


FIG. 2. Correlation between CGES-based indicators and plasticity across six model systems. Columns display the following: (1) CGES contour plots; (2) Derived structural indicator [y gradient for single crystals, panels (a) and (b); divergence for disordered systems, panels (c)–(f)]; (3) Nonaffine displacement field at 0.1% shear strain. Rows correspond to the following: (a) Cu single-edge dislocation, (b) Nb_3Sn single-edge dislocation, (c) polycrystalline Cu, (d) polycrystalline Nb_3Sn, (e) icosahedral quasicrystal, and (f) KA amorphous alloy.

f_{cov}. The goal is to select an optimal f_{cov} that maximizes the predictive power for plastic events without overlabeling the system. The optimization strategy proposed by Rottler *et al.* [62], which evaluates the efficiency of soft zones in capturing high-strain atoms relative to random selection, is adopted.

Let f_{sat} denote the fraction of high-strain atoms (those involved in plastic events, i.e., STZs) that fall within the identified soft zones. If soft zones were uncorrelated with plasticity, one would expect $f_{sat} \approx f_{cov}$. The difference $f_{sat} - f_{cov}$ thus quantifies the excess predictive capability. This difference is plotted in Fig. 3(a) as a function of f_{cov} for our four disordered models. In all cases, the curve rises initially, indicating that the atoms with the highest CGES divergence are strongly correlated with plasticity. The curve then exhibits a maximum, representing the optimal balance point where the soft zone population captures the majority of plastic events with minimal f_{cov}. Beyond this peak, adding more atoms (increasing f_{cov}) yields diminishing returns as less relevant regions are included. Based on these maxima, the optimal f_{cov} is determined to be approximately 14% for polycrystalline Cu, 20% for Nb_3Sn, 19% for the quasicrystal, and 24% for the KA amorphous system.

To further understand the efficiency of prediction, the ratio f_{sat}/f_{cov} is analyzed. How this ratio evolves with increasing soft zone coverage is shown in Fig. 3(b). At very low f_{cov}, the ratio is high, confirming that the "softest" atoms are extremely likely to participate in plastic events. As f_{cov} increases, the ratio monotonically decays towards unity (random correlation). The selected thresholds (near the knee of these curves) are conservative. They prioritize the most vulnerable structural defects that act as nucleation sites for plasticity, rather than attempting to encompass all regions that might eventually yield during avalanche propagation. This focus on nucleation is crucial for predicting the onset of failure.

C. Quantitative correlation with plasticity

To substantiate the visual correspondence established in the previous section, the correlation between identified soft zones and plastic events is quantified. Single dislocation models are excluded from this probabilistic analysis because, in crystals containing mobile dislocations under resolved shear stress, plasticity is deterministically and exclusively mediated by dislocation cores. The occurrence probability of a plastic event outside the core region is effectively zero under standard deformation conditions, rendering a statistical enrichment metric inapplicable. Therefore, the focus is on the four disordered systems: polycrystalline Cu and Nb_3Sn, quasicrystals, and KA amorphous alloys.

The von Mises atomic strain [63] is employed to define plastic events. Since atomic strain magnitudes vary across systems, atomic strains are normalized by the system maximum. Atoms exceeding a normalized strain threshold are identified as participating in plastic events. To evaluate prediction accuracy, the probability ratio is defined as [62]

$$\frac{f_{ss}}{f_{cov}}. \tag{3}$$

Here, f_{ss} is the fraction of high-strain atoms located within soft zones relative to the total high-strain population, and

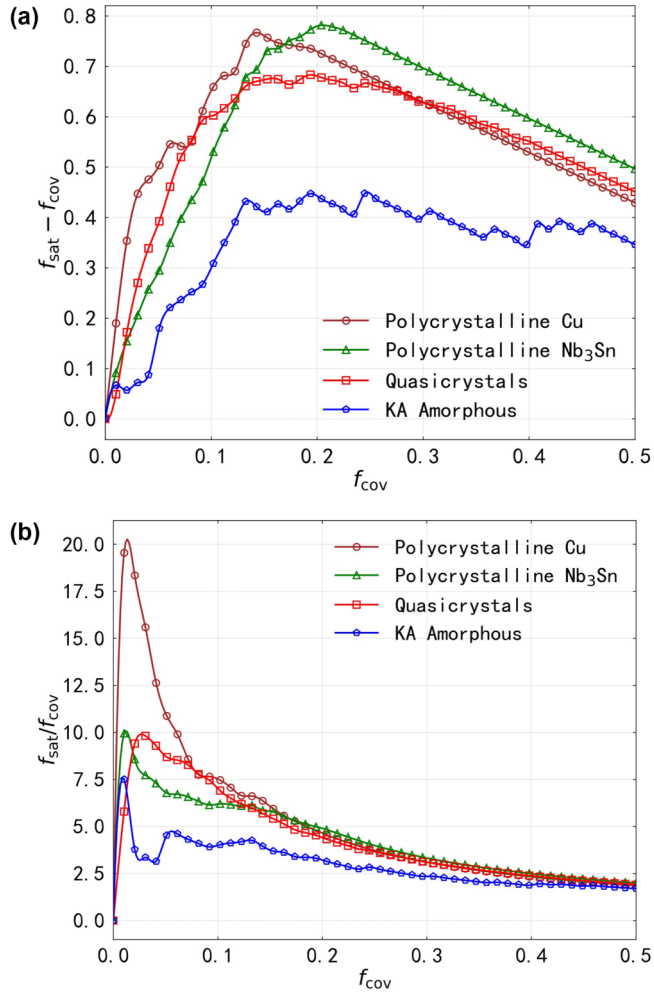


FIG. 3. Determination of the soft zone. (a) Optimization of soft zone coverage. The difference between the fraction of captured plastic events (f_{sat}) and the soft zone volume fraction (f_{cov}) is plotted against f_{cov}. The peak indicates the optimal threshold for identifying structural defects. (b) Efficiency of soft zone prediction. The ratio f_{sat}/f_{cov} decreases as the definition of soft zones is broadened. High values at low coverage confirm that atoms with the highest CGES divergence are primary carriers of plasticity.

f_{cov} is the fraction of the total system volume identified as soft zones (see Sec. III B). Note that while f_{sat} (introduced in Sec. III B) and f_{ss} share a similar mathematical form (fraction of high-strain atoms in soft zones), they differ fundamentally in their constraints: f_{sat} varies with the soft zone coverage (f_{cov}) under a fixed definition of high strain, whereas f_{ss} here varies with the strain threshold definition under a fixed f_{cov} determined in Sec. III B. A ratio exceeding 1 indicates positive correlation, while unity implies random correlation.

The evolution of f_{ss}/f_{cov} as a function of normalized strain threshold is presented in Fig. 4. At zero threshold, the ratio approaches unity, as expected. However, as the threshold increases to isolate significant plastic events, the ratio rises sharply and saturates at elevated levels. Specifically, the ratios for polycrystalline Cu and polycrystalline Nb_3Sn saturate at ∼7 and ∼5, respectively, when the normalized strain threshold reaches or exceeds 0.3 and 0.4. For the quasicrystal and the KA amorphous system, the ratios saturate near ∼5 and ∼3 when the normalized strain reaches or exceeds 0.7 and 0.8, respectively. It is indicated by these high ratios that plastic events are 3–7 times more likely to originate within the soft zones identified by CGES divergence than in the bulk and that CGES divergence is not merely a visual marker but a robust structural indicator of plastic instability under AQS loading in the disordered systems studied.

D. Alignment of soft zone eigenvectors

To reveal the microscopic mechanism by which soft zones facilitate plastic rearrangements, the directional alignment between the local structural propensity and the actual plastic response is quantified. The tensorial correlation $\frac{3}{2}\mathrm{tr}(\mathbf{E}^{(i)}\mathbf{V})$ is employed, where $\mathbf{E}^{(i)}$ and $\mathbf{V}$ are nematic tensors constructed from the ith normalized soft-mode eigenvector $\hat{\mathbf{e}}^{(i)}$ ($i = 1$, 2, and 3) of local dynamical matrix and the nonaffine displacement vector $\hat{\mathbf{v}}$, respectively [62]. The components are defined as

$$E^{(i)}_{\alpha\beta} = \hat{e}^{(i)}_{\alpha}\hat{e}^{(i)}_{\beta} - \tfrac{1}{3}\delta_{\alpha\beta},$$
$$V_{\alpha\beta} = \hat{v}_{\alpha}\hat{v}_{\beta} - \tfrac{1}{3}\delta_{\alpha\beta}. \quad (4)$$

Here, α and β denote Cartesian components (x, y, z), and $\delta_{\alpha\beta}$ is the Kronecker delta. The trace is normalized by the prefactor 3/2 such that the correlation ranges from 0 (random orientation) to 1 (perfect alignment).

The evolution of this correlation averaged over soft zone atoms for the three frequency modes ($i = 1$, 2, and 3) of the local dynamic matrix as a function of the normalized strain threshold is displayed in Fig. 5. Remarkably, even at the limit of zero normalized strain threshold, where all soft zone atoms are included regardless of their plastic participation, the alignment is substantial (0.38–0.45) across all four disordered systems. This indicates a robust intrinsic correlation. Even under minute deformations, the atomic displacements are biased towards the directions encoded in the preexisting soft eigenvectors. As the threshold increases to selectively filter for high-strain plastic events, the correlation exhibits a sustained upward trend. It is confirmed that the most intense plastic rearrangements occur along the paths dictated by the local dynamical matrix, demonstrating that the polarization of incipient plastic rearrangements is effectively predicted by the local eigenvectors.

E. Validity regime of CGES

The present work validates CGES exclusively under AQS conditions, which probe the local curvature of the PEL at zero temperature without thermal fluctuations. It is therefore important to carefully delineate the physical regime in which CGES constitutes a valid predictor and to distinguish it from thermally activated plasticity. This distinction is especially important in light of the rich multiscale barrier structure known to govern disordered systems.

Within the PEL framework, D_i^* is related to the local curvature of the energy basin in which atom i resides. In the harmonic approximation underlying the Einstein model, the local free energy reads $F_i \propto k_B T \ln(\hbar\omega_i/k_B T)$, where $\omega_i \sim |D_i|^{1/6}$ [59,60]. In the present analysis,

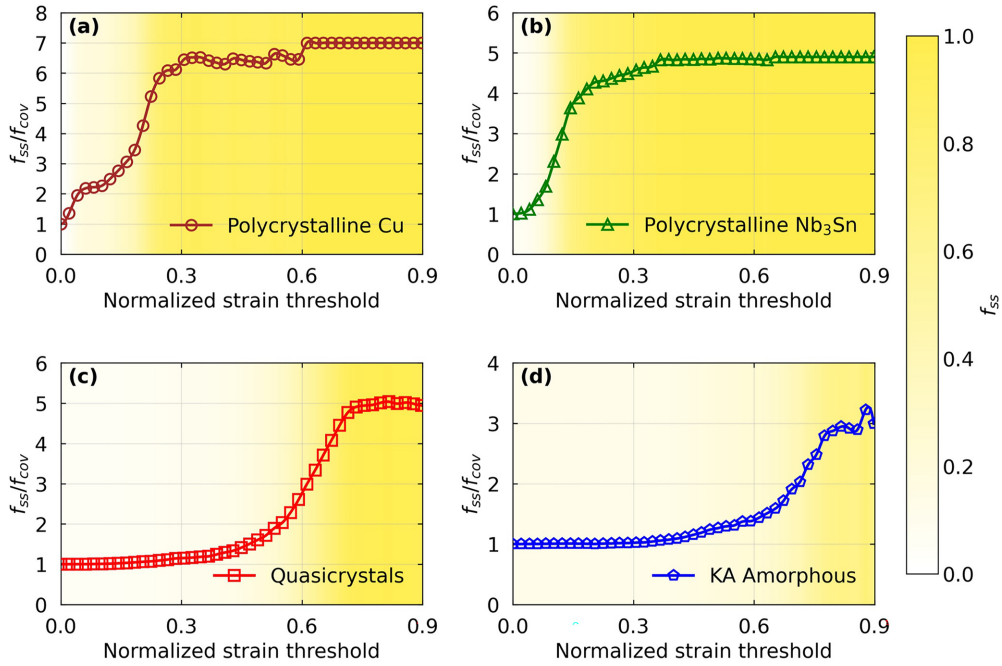


FIG. 4. Ratio of proportion of high-strain atoms in soft zones to soft zone coverage as a function of normalized strain threshold. (a) Polycrystalline Cu, (b) polycrystalline Nb_3Sn, (c) quasicrystal, and (d) KA amorphous system. Normalized strain values exceeding 0.9 are excluded to avoid errors.

however, plasticity-prone regions are not identified from the absolute value of D_i^* alone. Instead, they are extracted from spatial variations of the CGES field. These derivative fields highlight local stiffness heterogeneity and defectlike environments. Under AQS conditions, the regions selected by these CGES-derived indicators are statistically more likely to undergo local instabilities, consistent with prior correlations between stiffnesslike structural descriptors

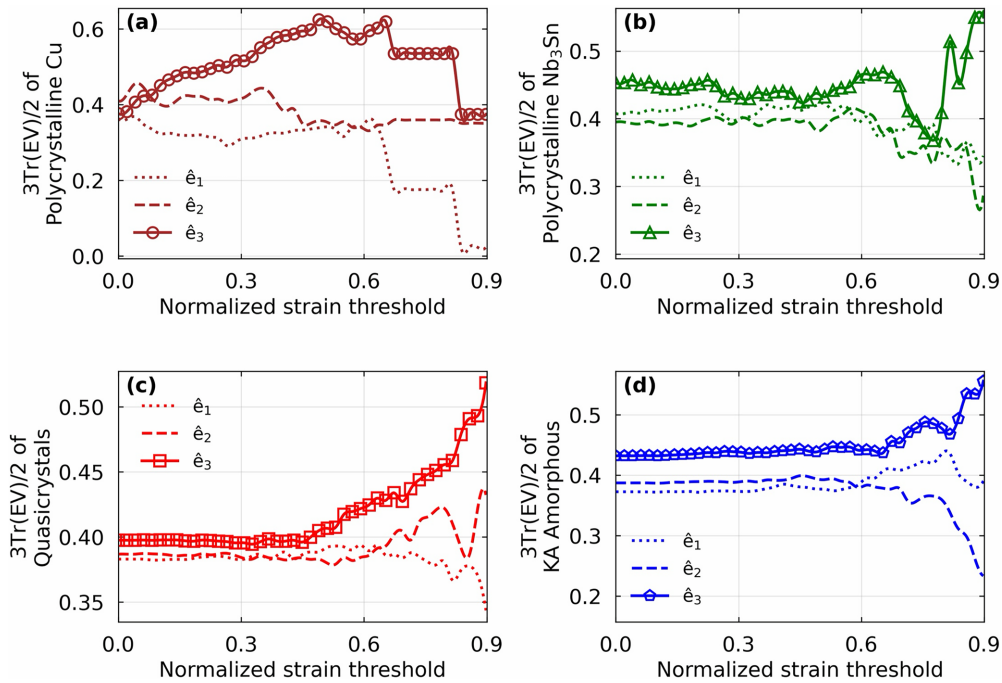


FIG. 5. Curves showing the tensorial correlation $\frac{3}{2}\mathrm{tr}(\mathbf{E}^{(i)}\mathbf{V})$ as a function of normalized strain. $\mathbf{E}^{(i)}$ and $\mathbf{V}$ represent the ith eigenvector ($i = 1,\ 2,$ and 3) and nonaffine displacement tensors, respectively. The components are defined as $E^{(i)}_{\alpha\beta} = \hat{e}^{(i)}_{\alpha}\hat{e}^{(i)}_{\beta} - \delta_{\alpha\beta}/3$ and $V_{\alpha\beta} = \hat{v}_{\alpha}\hat{v}_{\beta} - \delta_{\alpha\beta}/3$. Here, $\hat{e}^{(i)}$ and $\hat{v}$ denote the normalized eigenvector and the nonaffine displacement vector of atoms in the soft region. The dotted, dashed, and solid lines correspond to eigenvectors $i = 1,\ 2,$ and 3, respectively.

and shear transformations in metallic glasses [28–30]. The probability ratios of 3–7 observed in Sec. III C therefore support the use of CGES-derived fields as useful structural indicators of athermal plastic initiation in the systems studied.

This interpretation has an important limitation. The energy landscape of disordered solids presents barriers of qualitatively different character depending on the temperature and driving stress, a point thoroughly established in the framework of elastic manifold depinning in disordered media [64,65]. At zero temperature and finite applied stress, plastic flow is controlled by localized, instantaneous barriers associated with individual pinning events, which are the barriers directly probed under AQS conditions. At low stress and finite temperature, however, thermally activated creep is governed by entirely different, collective barriers. These involve the correlated bypassing of many disorder centers and are spatially extended, flat-topped, and much larger in scale than the instantaneous barriers [64,65]. These two barrier types differ not only in height and spatial extent but also in their fundamental physical origin, and neither can be directly inferred from the other. The stiffness argument applicable in the athermal limit therefore does not carry over to the creep regime.

This separation of barrier regimes is of direct relevance to several material classes studied in the broader plasticity literature. In disordered crystals such as solid solutions and high entropy alloys, the barriers controlling thermally activated dislocation motion have been shown by Varvenne, Curtin, and co-workers to arise from the collective interaction of a dislocation line with a statistically fluctuating solute field over extended length scales [66–68], rather than from local stiffness at individual atomic sites, which is a manifestation of the collective, extended barrier regime identified in elastic manifold theory. Similarly, theoretical treatments of stress-driven avalanche phenomena and the yielding transition in amorphous solids draw conceptual connections to the elastic manifold depinning framework [69,70], a picture that explicitly relies on the existence of barriers on multiple scales, in which local stiffness alone determines rearrangement susceptibility, would not be consistent with this body of work.

We therefore emphasize that the CGES framework, as validated here, should be understood as a descriptor of athermal plasticity. Its strong predictive power in this regime does not extend, in general, to thermally activated low-stress creep, where collective barrier mechanisms are dominant and local stiffness is not a sufficient predictor. This boundary is a deliberate scope of the present work rather than a weakness of CGES as an athermal indicator. Extending the CGES framework to finite-temperature creep and establishing its relation to activation energies across both barrier regimes constitute important directions for future work.

IV. SUMMARY

Based on the local dynamical matrix, coarse-grained equivalent stiffness (CGES) is introduced as a broadly applicable structural parameter to quantify local mechanical stability. Structural defects susceptible to plastic rearrangement are effectively delineated by the spatial distribution of CGES and its gradient or divergence. The broad applicability of CGES is demonstrated through systematic AQS shear simulations across six model systems, ranging from single crystals with dislocations to disordered polycrystals, quasicrystals, and amorphous solids.

Qualitatively, the identified soft zones exhibit remarkable spatial coincidence with regions of intense nonaffine displacement, accurately locating dislocation cores, grain boundaries, and shear transformation zones. In single crystals, the CGES gradient deterministically identifies dislocation cores, where plasticity is exclusively localized. In the four disordered systems studied, plastic events are statistically concentrated within the CGES-identified soft zones, with occurrence probabilities 3–7 times higher than those in the bulk. Furthermore, significant alignment with the actual plastic flow directions is displayed by the low-frequency eigenvectors associated with these soft zones, revealing the microscopic pathways of deformation.

Within the AQS conditions considered here, CGES provides a computation-efficient structural framework for identifying defectlike, plasticity-prone regions without requiring *a priori* knowledge of deformation. It offers a microscopic basis for understanding the origins of localized failure across diverse classes of solids.

ACKNOWLEDGMENTS

This work was supported by the National Natural Science Foundation of China (Grants No. 12302082 and No. 12472112). This reaserch was funded in whole or in part by the Austrian Science Fund (FWF) (Grant No. 10.55776/PAT6731223). This work was also supported by the Joint Fund of Henan Province Science and Technology R&D Program (Grant No. 235200810062), the Mid-to-Long-Term Visiting Scholar Program of Henan Academy of Sciences (Project No. 20262617001), and the Startup Research Fund of Henan Academy of Sciences (Project No. 231817007).

DATA AVAILABILITY

The data that support the findings of this article are openly available [71].

[1] X. Li, Z. Zhang, and J. Wang, Deformation twinning in body-centered cubic metals and alloys, Prog. Mater. Sci. **139**, 101160 (2023).

[2] W.-H. Wang *et al.*, Metallic glass roadmap, Mater. Futures **4**, 033001 (2025).

[3] P. Morse, S. Wijtmans, M. Van Deen, M. Van Hecke, and M. L. Manning, Differences in plasticity between hard and soft spheres, Phys. Rev. Res. **2**, 023179 (2020).

[4] L. Berthier, G. Biroli, M. L. Manning, and F. Zamponi, Yielding and plasticity in amorphous solids, Nat. Rev. Phys. **7**, 313 (2025).

[5] F. Spaepen, A microscopic mechanism for steady state inhomogeneous flow in metallic glasses, Acta Metall. **25**, 407 (1977).

[6] P. Schall, D. A. Weitz, and F. Spaepen, Structural rearrangements that govern flow in colloidal glasses, Science **318**, 1895 (2007).
[7] C. Zhong, H. Zhang, Q. P. Cao, X. D. Wang, D. X. Zhang, U. Ramamurty, and J. Z. Jiang. Deformation behavior of metallic glasses with shear band like atomic structure: A molecular dynamics study, Sci. Rep. **6**, 30935 (2016).
[8] A. Baranyai and D. J. Evans, Direct entropy calculation from computer simulation of liquids, Phys. Rev. A **40**, 3817 (1989).
[9] M. Leocmach, J. Russo, and H. Tanaka, Importance of many-body correlations in glass transition: An example from polydisperse hard spheres, J. Chem. Phys. **138**, 12A536 (2013).
[10] X. Yang, R. Liu, M. Yang, W.-H. Wang, and K. Chen, Structures of local rearrangements in soft colloidal glasses, Phys. Rev. Lett. **116**, 238003 (2016).
[11] P. M. Piaggi and M. Parrinello, Entropy based fingerprint for local crystalline order, J. Chem. Phys. **147**, 114112 (2017).
[12] T. Kawasaki, T. Araki, and H. Tanaka, Correlation between dynamic heterogeneity and medium-range order in two-dimensional glass-forming liquids, Phys. Rev. Lett. **99**, 215701 (2007).
[13] C. F. Schreck, C. S. O'Hern, and L. E. Silbert, Tuning jammed frictionless disk packings from isostatic to hyperstatic, Phys. Rev. E **84**, 011305 (2011).
[14] A. Widmer-Cooper, H. Perry, P. Harrowell, and D. R. Reichman, Irreversible reorganization in a supercooled liquid originates from localized soft modes, Nat. Phys. **4**, 711 (2008).
[15] J. Ding, S. Patinet, M. L. Falk, Y. Cheng, and E. Ma, Soft spots and their structural signature in a metallic glass, Proc. Natl. Acad. Sci. USA **111**, 14052 (2014).
[16] Y. C. Hu and H. Tanaka, Unveiling hidden particle-level defects in glasses, Nat. Commun. **16**, 5321 (2025).
[17] H. Tong and N. Xu, Order parameter for structural heterogeneity in disordered solids, Phys. Rev. E **90**, 010401(R) (2014).
[18] Y. C. Hu, F. X. Li, M. Z. Li, H. Y. Bai, and W. H. Wang, Five-fold symmetry as indicator of dynamic arrest in metallic glass-forming liquids, Nat. Commun. **6**, 8310 (2015).
[19] L. Mao-Zhi, State key laboratory for advanced metals and materials, university of science and technology beijing, beijing 100083, china. entropy and glass formation, Acta Phys. Sin. **66**, 176107 (2017).
[20] J. M. Rieser, C. P. Goodrich, A. J. Liu, and D. J. Durian, Divergence of Voronoi cell anisotropy vector: A threshold-free characterization of local structure in amorphous materials, Phys. Rev. Lett. **116**, 088001 (2016).
[21] J. Ding, Y. Q. Cheng, H. Sheng, M. Asta, R. O. Ritchie, and E. Ma, Universal structural parameter to quantitatively predict metallic glass properties, Nat. Commun. **7**, 13733 (2016).
[22] Z. Fan, J. Ding, Q.-J. Li, and E. Ma, Correlating the properties of amorphous silicon with its flexibility volume, Phys. Rev. B **95**, 144211 (2017).
[23] S. Patinet, D. Vandembroucq, and M. L. Falk, Connecting local yield stresses with plastic activity in amorphous solids, Phys. Rev. Lett. **117**, 045501 (2016).
[24] A. Barbot, M. Lerbinger, A. Hernandez-Garcia, R. García-García, M. L. Falk, D. Vandembroucq, and S. Patinet, Local yield stress statistics in model amorphous solids, Phys. Rev. E **97**, 033001 (2018).
[25] A. Barbot, M. Lerbinger, A. Lemaître, D. Vandembroucq, and S. Patinet, Rejuvenation and shear banding in model amorphous solids, Phys. Rev. E **101**, 033001 (2020).
[26] E. D. Cubuk, S. S. Schoenholz, E. Kaxiras, and A. J. Liu, Structural properties of defects in glassy liquids, J. Phys. Chem. B **120**, 6139 (2016).
[27] E. D. Cubuk, R. J. S. Ivancic, S. S. Schoenholz, D. J. Strickland, A. Basu, Z. S. Davidson, J. Fontaine, J. L. Hor, Y.-R. Huang, Y. Jiang, N. C. Keim, K. D. Koshigan, J. A. Lefever, T. Liu, X.-G. Ma, D. J. Magagnosc, E. Morrow, C. P. Ortiz, J. M. Rieser, A. Shavit, *et al.*, Structure-property relationships from universal signatures of plasticity in disordered solids, Science **358**, 1033 (2017).
[28] B. Xu, M. Falk, J. Li, and L. Kong, Strain-dependent activation energy of shear transformation in metallic glasses, Phys. Rev. B **95**, 144201 (2017).
[29] B. Xu, M. L. Falk, J. F. Li, and L. T. Kong, Predicting shear transformation events in metallic glasses, Phys. Rev. Lett. **120**, 125503 (2018).
[30] D. Wei, J. Yang, M. Q. Jiang, B. C. Wei, Y. J. Wang, and L. H. Dai, Revisiting the structure–property relationship of metallic glasses: Common spatial correlation revealed as a hidden rule, Phys. Rev. B **99**, 014115 (2019).
[31] J. Zylberg, E. Lerner, Y. Bar-Sinai, and E. Bouchbinder, Local thermal energy as a structural indicator in glasses, Proc. Natl. Acad. Sci. USA **114**, 7289 (2017).
[32] Z. Schwartzman-Nowik, E. Lerner, and E. Bouchbinder, Anisotropic structural predictor in glassy materials, Phys. Rev. E **99**, 060601(R) (2019).
[33] H. Tong and H. Tanaka, Revealing hidden structural order controlling both fast and slow glassy dynamics in supercooled liquids, Phys. Rev. X **8**, 011041 (2018).
[34] B. Shang, P. Guan, and J.-L. Barrat, Role of thermal expansion heterogeneity in the cryogenic rejuvenation of metallic glasses, J. Phys. Mater. **1**, 015001 (2018).
[35] Y. Wu, B. Xu, X. Zhang, and P. Guan, Machine-learning inspired density-fluctuation model of local structural instability in metallic glasses, Acta Mater. **247**, 118741 (2023).
[36] B. Huang, T. P. Ge, G. L. Liu, J. H. Luan, Q. F. He, Q. X. Yuan, W. X. Huang, K. Zhang, H. Y. Bai, C. H. Shek, C. T. Liu, Y. Yang, and W. H. Wang, Density fluctuations with fractal order in metallic glasses detected by synchrotron X-ray nano-computed tomography, Acta Mater. **155**, 69 (2018).
[37] J. Yang, Y. J. Wang, E. Ma, A. Zaccone, L. H. Dai, and M. Q. Jiang, Structural parameter of orientational order to predict the Boson vibrational anomaly in glasses, Phys. Rev. Lett. **122**, 015501 (2019).
[38] M. Baggioli, I. Kriuchevskyi, T. W. Sirk, and A. Zaccone, Plasticity in amorphous solids is mediated by topological defects in the displacement field, Phys. Rev. Lett. **127**, 015501 (2021).
[39] B. Xu, M. L. Falk, S. Patinet, and P. Guan, Atomic nonaffinity as a predictor of plasticity in amorphous solids, Phys. Rev. Mater. **5**, 025603 (2021).
[40] Z. Fan and E. Ma, Predicting orientation-dependent plastic susceptibility from static structure in amorphous solids via deep learning, Nat. Commun. **12**, 1506 (2021).
[41] Z. Fan, E. Ma, and M. L. Falk, Predicting the location of shear band initiation in a metallic glass, Phys. Rev. Mater. **6**, 065602 (2022).

[42] D. Şopu, A. Stukowski, M. Stoica, and S. Scudino, Atomic-level processes of shear band nucleation in metallic glasses, Phys. Rev. Lett. **119**, 195503 (2017).

[43] D. Şopu, STZ-Vortex model: The key to understand STZ percolation and shear banding in metallic glasses, J. Alloys Compd. **960**, 170585 (2023).

[44] Z. W. Wu, Y. Chen, W.-H. Wang, W. Kob, and L. Xu, Topology of vibrational modes predicts plastic events in glasses, Nat. Commun. **14**, 2955 (2023).

[45] A. Bera, A. Zaccone, and M. Baggioli, Hedgehog topological defects in 3D amorphous solids, Nat. Commun. **16**, 5990 (2025).

[46] L.-Z. Huang, Y.-J. Wang, M.-Q. Jiang, and M. Baggioli, Spotting structural defects in crystals from the topology of vibrational modes, J. Mech. Phys. Solids **204**, 106274 (2025).

[47] M. L. Manning and A. J. Liu, Vibrational modes identify soft spots in a sheared disordered packing, Phys. Rev. Lett. **107**, 108302 (2011).

[48] R.-H. Shi, Defects identifier based on coarse grained equivalent stiffness gradient in 2D metallic glasses, Mater. Today Commun. **35**, 106100 (2023).

[49] R.-H. Shi, P. Xiao, R. Yang, and Y.-L. Bai, Atomic-level structural identification for prediction of localized shear deformation in metallic glasses, Int. J. Solids Struct. **191-192**, 363 (2020).

[50] A. Lemaître and C. Maloney, Sum rules for the quasi-static and visco-elastic response of disordered solids at zero temperature, J. Stat. Phys. **123**, 415 (2006).

[51] P. Hirel, Atomsk: A tool for manipulating and converting atomic data files, Comput. Phys. Commun. **197**, 212 (2015).

[52] S. M. Rassoulinejad-Mousavi, Y. Mao, and Y. Zhang, Evaluation of copper, aluminum, and nickel interatomic potentials on predicting the elastic properties, J. Appl. Phys. **119**, 244304 (2016).

[53] S.-H. Oh, D. Seol, Y.-J. Jeong, S.-H. Na, J. Kim, W.-S. Ko, J. B. Jeon, and B.-J. Lee, Diffusion in A15 Nb_3Sn: An atomistic study, Acta Mater. **234**, 118050 (2022).

[54] A. P. Thompson, H. M. Aktulga, R. Berger, D. S. Bolintineanu, W. M. Brown, P. S. Crozier, P. J. in 't Veld, A. Kohlmeyer, S. G. Moore, T. D. Nguyen, R. Shan, M. J. Stevens, J. Tranchida, C. Trott, and S. J. Plimpton, LAMMPS - a flexible simulation tool for particle-based materials modeling at the atomic, meso, and continuum scales, Comput. Phys. Commun. **271**, 108171 (2022).

[55] A. Stukowski, Visualization and analysis of atomistic simulation data with OVITO–The Open Visualization Tool, Modell. Simul. Mater. Sci. Eng. **18**, 015012 (2010).

[56] M. Mihalkovič and C. L. Henley, Empirical oscillating potentials for alloys from *ab initio* fits and the prediction of quasicrystal-related structures in the Al-Cu-Sc system, Phys. Rev. B **85**, 092102 (2012).

[57] L.-L. Cao, K. Zhao, and Y.-J. Wang, Phonon dynamics in 3D quasicrystals versus amorphous solids, J. Appl. Phys. **137**, 055104 (2025).

[58] W. Kob and H. C. Andersen, Testing mode-coupling theory for a supercooled binary Lennard-Jones mixture I: The van Hove correlation function, Phys. Rev. E **51**, 4626 (1995).

[59] R. LeSar, R. Najafabadi, and D. J. Srolovitz, Finite-temperature defect properties from free-energy minimization, Phys. Rev. Lett. **63**, 624 (1989).

[60] P. Xiao, J. Wang, F. J. Ke, and Y. L. Bai, Molecular statistical thermodynamics–A distinct and efficient numerical approach to quasi-static analysis of nanomaterials at finite temperature, Composites, Part B **43**, 57 (2012).

[61] Z.-Y. Yang, Y.-J. Wang, and A. Zaccone, Correlation between vibrational anomalies and emergent anharmonicity of the local potential energy landscape in metallic glasses, Phys. Rev. B **105**, 014204 (2022).

[62] J. Rottler, S. S. Schoenholz, and A. J. Liu, Predicting plasticity with soft vibrational modes: From dislocations to glasses, Phys. Rev. E **89**, 042304 (2014).

[63] F. Shimizu, S. Ogata, and J. Li, Theory of shear banding in metallic glasses and molecular dynamics calculations, Mater. Trans. **48**, 2923 (2007).

[64] D. S. Fisher, Collective transport in random media: From superconductors to earthquakes, Phys. Rep. **301**, 113 (1998).

[65] E. E. Ferrero, L. Foini, T. Giamarchi, A. B. Kolton, and A. Rosso, Creep motion of elastic interfaces driven in a disordered landscape, Annu. Rev. Condens. Matter Phys. **12**, 111 (2021).

[66] C. Varvenne, A. Luque, and W. A. Curtin, Theory of strengthening in fcc high entropy alloys, Acta Mater. **118**, 164 (2016).

[67] C. Varvenne, G. P. M. Leyson, M. Ghazisaeidi, and W. A. Curtin, Solute strengthening in random alloys, Acta Mater. **124**, 660 (2017).

[68] G. P. M. Leyson, W. A. Curtin, L. G. Hector, Jr., and C. F. Woodward, Quantitative prediction of solute strengthening in aluminium alloys, Nat. Mater. **9**, 750 (2010).

[69] J. Lin, E. Lerner, A. Rosso, and M. Wyart, Scaling description of the yielding transition in soft amorphous solids at zero temperature, Proc. Natl. Acad. Sci. USA **111**, 14382 (2014).

[70] M. Müller and M. Wyart, Marginal stability in structural, spin, and electron glasses, Annu. Rev. Condens. Matter Phys. **6**, 177 (2015).

[71] C.-W. Bian, L.-L. Cao, R.-H. Shi, D. Şopu, and Y.-J. Wang, Data for "Coarse-grained equivalent stiffness: A structure-plasticity indicator across the order-disorder spectrum", version V1 (Science Data Bank, 2026), https://doi.org/10.57760/sciencedb.28192; direct access: https://www.scidb.cn/en/s/yaQJRz.